Earthquake swarms on transform faults

Emily Roland[1] and Jeffrey J. McGuire[2]

[1] *MIT-WHOI Joint Program, Woods Hole,* MA 02543, *USA. E-mail: eroland@mit.edu*
[2] *Woods Hole Oceanographic Institution, Woods Hole,* MA 02543, *USA*

SUMMARY

Swarm-like earthquake sequences are commonly observed in a diverse range of geological settings including volcanic and geothermal regions as well as along transform plate boundaries. They typically lack a clear mainshock, cover an unusually large spatial area relative to their total seismic moment release, and fail to decay in time according to standard aftershock scaling laws. Swarms often result from a clear driving phenomenon, such as a magma intrusion, but most lack the necessary geophysical data to constrain their driving process. To identify the mechanisms that cause swarms on strike-slip faults, we use relative earthquake locations to quantify the spatial and temporal characteristics of swarms along Southern California and East Pacific Rise transform faults. Swarms in these regions exhibit distinctive characteristics, including a relatively narrow range of hypocentral migration velocities, on the order of a kilometre per hour. This rate corresponds to the rupture propagation velocity of shallow creep transients that are sometimes observed geodetically in conjunction with swarms, and is significantly faster than the earthquake migration rates typically associated with fluid diffusion. The uniformity of migration rates and low effective stress drops observed here suggest that shallow aseismic creep transients are the primary process driving swarms on strike-slip faults. Moreover, the migration rates are consistent with laboratory values of the rate-state friction parameter b (0.01) as long as the Salton Trough faults fail under hydrostatic conditions.

Key words: Creep and deformation; Earthquake source observations; Transform faults.

GJI Tectonics and geodynamics

1 INTRODUCTION

The term 'earthquake swarm' typically refers to a cluster of moderate earthquakes that occur over a period of hours to days without a distinct mainshock. In regions of magma intrusion and CO_2 degassing, swarms have been linked to fluid-flow processes that alter the stress field and trigger seismicity (Hill 1977; Smith *et al.* 2004; Hainzl & Ogata 2005). However, with recent improvements in seismic observation capabilities, it is becoming clear that swarms occur in a variety of tectonic settings, not just in areas of volcanism. High rates of seismic swarms have been observed historically in the southern region of the San Andreas transform fault system, where it extends into the Salton Trough in Southern California (Richter 1958; Brune & Allen 1967; Johnson & Hadley 1976). Recent studies of high-quality earthquake catalogues have demonstrated that swarms are a common feature of various large-scale tectonic fault systems including those in California and Japan (Vidale & Shearer 2006; Vidale *et al.* 2006). Additionally, analysis of aftershock productivity and foreshock occurrence rates on mid-ocean ridge transform faults indicates that oceanic sequences are generally more swarm-like than typical sequences on continental strike-slip boundaries (McGuire *et al.* 2005).

Although in may cases, geophysical observations are not available to constrain the specific process, certain swarm seismicity characteristics reflect an underlying driving mechanism that is fundamentally different from mainshock–aftershock Coulomb stress triggering. Earthquake swarms are often characterized by an effective seismic stress drop (the ratio of total seismic moment release to fault area) that is an order of magnitude lower than stress drop values typical for mainshock–aftershock sequences on strike-slip faults (Vidale & Shearer 2006). Empirical laws developed from observations of aftershock sequences triggered from a single large event also do a poor job of fitting swarms on transform boundaries. Omori's Law of seismicity rate decay following a main shock (Omori 1894) and Båth's law, which describes the difference in the magnitude of a mainshock and its largest aftershock (Helmstetter & Sornette 2003b), cannot be applied to earthquake swarm seismicity with parameters typical of continental strike-slip fault systems. The unusual temporal and spatial seismicity patters associated with swarms on continental faults are also observed for earthquake sequences on the East Pacific Rise (EPR). McGuire *et al.* (2005) showed that foreshocks are an order of magnitude more common on EPR transform faults than on faults in California, while aftershocks are an order of magnitude less common. This analysis demonstrated that EPR transform seismicity cannot be explained by typical earthquake triggering models, and suggested that an aseismic driving process was likely responsible for the increased foreshock activity. Forsyth *et al.* (2003), inferred an anomalously low stress drop associated with a swarm on the

western boundary of the Easter Microplate. An aseismic slip event was similarly hypothesized as the triggering phenomenon driving the seismicity there based on the unusual spatial properties of the swarm.

A few studies have directly associated swarms on transform faults with geodetically observed aseismic creep. On the central San Andreas, Linde *et al.* (1996) used creepmeter observations to connect a small number of earthquakes with magnitude ~5 creep events that had timescales of a few days. Lohman & McGuire (2007) studied a large swarm in the Salton Trough using both seismic and geodetic data, and inferred that the magnitude of surface deformation that occurred during the swarm could not be explained by the recorded seismicity alone. Modelling of the observed deformation required a significant contribution from shallow aseismic creep coincident with the swarm. A hypocentral migration velocity on the order of $0.5 \, \text{km} \, \text{hr}^{-1}$, which was observed during the early stage of the Lohman and McGuire sequence is a common feature of strike-slip swarms in the Salton Trough (Johnson & Hadley 1976). This velocity is consistent with estimated rupture propagation speeds of creep events in California (King *et al.* 1973; Burford 1977; Linde *et al.* 1996; Glowacka *et al.* 2001) and along-strike migration rates associated with episodic slow slip events at subduction zones. Observations of tremor and episodic slow slip along Cascadia (McGuire & Segall 2003; Dragert *et al.* 2006; Kao *et al.* 2006) and in Japan (Obara 2002) have been used to determine along-strike migration velocities between 0.2 and $0.7 \, \text{km} \, \text{hr}^{-1}$ ($5-15 \, \text{km} \, \text{d}^{-1}$) for episodes with durations between 5 and 20 d and equivalent moment magnitudes of approximately 6.5–6.8. The $0.1-1.0 \, \text{km} \, \text{hr}^{-1}$ migration rate associated with aseismic fault slip and slow events is significantly faster than the migration rate of earthquakes observed in regions of CO_2 degassing and borehole fluid injections. Seismicity initiated by fluid overpressure tends to reflect fluid diffusion timescales, with earthquakes spreading spatially proportional to $t^{1/2}$ and migration velocities not exceeding fractions of a kilometre per day (Audigane *et al.* 2002; Hainzl & Ogata 2005; Shapiro *et al.* 2005). Based on the disparity between migration rates associated with fluid diffusion and aseismic slip, hypocentral migration velocities observed during seismic swarms may be used to infer the specific stress transfer mechanism driving seismicity, even if direct observational evidence of the mechanism is not available.

Here, we continue to investigate the physical mechanisms that cause earthquake swarms, and explore the possibility that swarms on strike-slip plate boundaries are generally associated with aseismic creep. In this study, seven swarms are analysed from Southern California and EPR transform faults. Reliable earthquake locations are derived and are used to identify spatial migration patterns, which are taken as a proxy for the physical triggering mechanism driving the sequences. We employ temporal characteristics of the moment release to develop an objective definition of an earthquake swarm, and identify spatial moment release characteristics that are common to most swarms in our data set. We utilize estimates of hypocentral migration rate and the effective stress drop to constrain the potential mechanism causing swarms on strike-slip faults in Southern California and the EPR, and compare our results to predictions calculated from rate-state friction and crack propagation models.

2 DATA AND METHODS

We systematically explore the physical mechanisms causing tectonic swarms by analysing a number of sequences from the Salton Trough and Pacific transforms. Owing to the vast difference in

the quality and density of seismic data available, sequences from these two regions are analysed with different relocation methods. Seven earthquake sequences are analysed in total: three in Southern California that have accurate relocations available from prior studies, one in Southern California that we relocate using body waves recorded by local arrays and three oceanic transform sequences that are detected and located using teleseismic surface wave arrivals at Global Seismic Network (GSN) stations (Fig. 1). Using event locations and magnitudes, we estimate the effective stress drop and along-fault hypocentral migration rate of each swarm. We also calculate the skew of the temporal history of seismic moment release for each episode, which is used as a quantitative way to distinguish swarms from aftershock sequences. Below we describe the details of each calculation.

2.1 Southern California seismicity: body wave relocations

For each Southern California swarm analysed here, relative hypocentral locations were derived using body wave arrival times from local seismometer arrays. A swarm in 1975 was relocated by Johnson & Hadley (1976), and locations were derived for two swarms in 1981 and 2005 by Lohman & McGuire (2007). Migration velocities reported here are obtained using event locations from these two analyses. For a swarm in the Imperial fault zone in 2003, arrival time data was combined from two catalogues to determine relative relocations using the double-difference algorithm (Waldhauser & Ellsworth 2000). Arrival time picks from the Southern California Earthquake Data Center (SCEDC) were combined with arrivals from the Seismic Network of the Northwest Mexico (RESNOM), maintained by the 'Centro de Investigación Científica y de Educación Superior de Ensenada' (CICESE), which provided additional azimuthal coverage south of the US–Mexico border (Castro 1998). For the Imperial fault double-difference relocations, we required event arrival pairs to be observed at a minimum of eight stations within 500 km and separated by no more than 5 km. We employed a 1-D velocity model appropriate for the Salton Trough, which was extracted from the Southern California Earthquake Center's 3-D unified Southern California reference velocity model, version 4 (Magistrale *et al.* 2000).

2.2 EPR seismicity: surface wave relocation

We analyse three swarms from transform faults on the EPR and the Galapagos Ridge (Fig. 1) using a surface wave earthquake detection and location method that makes use of Rayleigh wave empirical Green's functions (EGFs). In the frequency band between 0.02 and 0.05 Hz, first-orbit Raleigh (R1) waves have a high signal-to-noise ratio and a group velocity that is fairly constant for young oceanic lithosphere, around $3.7 \, \text{km} \, \text{s}^{-1}$ (Nishimura & Forsyth 1988). This allows arrival times to be interpreted in terms of source location differences rather than dispersion (Forsyth *et al.* 2003). Waveforms from individual earthquakes on the same fault are essentially identical, and at low frequencies the amplitude of the waveforms scale with the moment of the earthquake. We identify and locate swarm events relative to an EGF based on their correlation coefficients and differential arrival times from a set of azimuthally distributed GSN stations. The magnitude and location of the selected EGF are taken from the Global Centroid Moment Tensor (CMT) catalogue directly when a CMT solution is available for one of the earthquakes in the sequence. If a moment calculation is not available, one of the large earthquakes in the sequence is cross-correlated with an appropriate
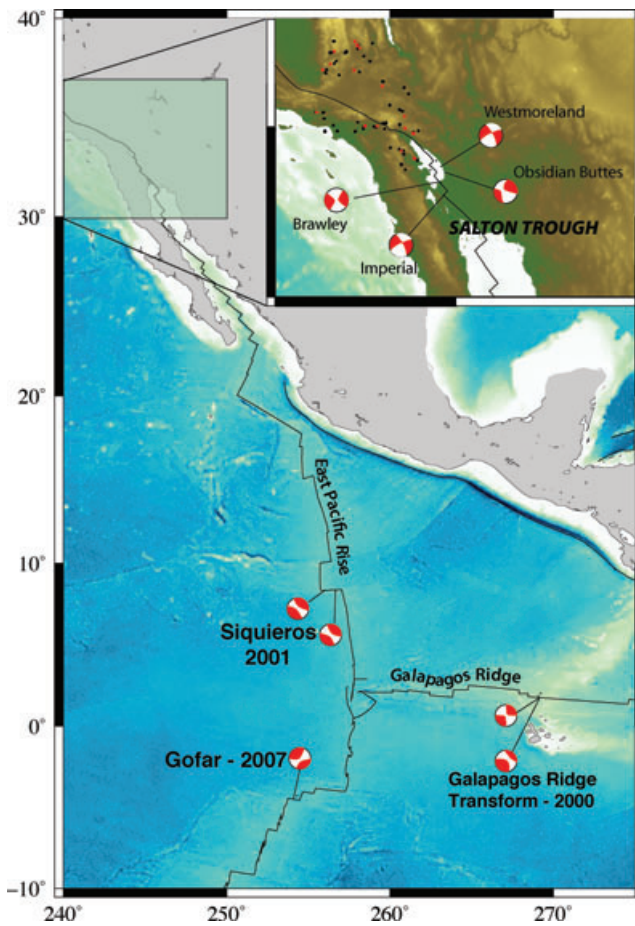
Figure 1. Strike-slip focal mechanisms from Global Centroid Moment Tensor (CMT) solutions representative of the three oceanic transform fault earthquakes analysed here: EPR sequences from the Siqueiros (2001) and Gofar (2007) transform faults, as well as the Galapagos Ridge transform (2000). Inlay map displays Southern California seismicity, including focal mechanisms representative of four Salton Trough swarms: Obsidian Buttes, West Moreland, Imperial fault and Brawley swarms. Dots show Southern California locations of seismic bursts identified by Vidale & Shearer (2006) as swarm-like (red dots) and those identified as aftershock sequences (black).

CMT catalogue event from the same fault to determine its seismic moment. That event is used as the EGF for the rest of the event locations. All of the EGF events used here are greater than M_w 4.7.

A swarm that occurred on the Galapagos Ridge transform in 2000 and a swarm on the Siqueiros transform in 2001 were detected by an array of autonomous hydrophones moored in the eastern equatorial Pacific maintained by NOAA (Fox *et al.* 2001). The earthquake catalogue derived from *t*-phases recorded by these hydrophones has a detection threshold of approximately M_w 3. We utilized these catalogues for identifying the source times of large swarm events. Magnitude estimates from the hydroacoustic catalogues are unreliable however, owing to complicated wave phenomena and the high-frequency energy of the *t*-phase (McGuire 2008). To determine reliable M_w estimates and locations, GSN waveforms for each *t*-phase event were extracted from a number of stations, bandpass filtered and cross-correlated with the EGF R1 waveform. Relative event locations were then obtained by fitting a cosine function to the differential R1 arrival times using an L1-norm fit. Best-fitting cosine scale and phase parameters characterize the distance and azimuth of the earthquake relative to the Green's function event (McGuire

2008). The location error is estimated using a bootstrap algorithm that assumes a Gaussian distribution with a 1 s standard deviation for the differential traveltime measurement errors (Shearer 1997; McGuire 2008). For the Gofar transform swarm that occurred in 2007, no events were detected by standard teleseismic catalogues. One of the sequence events was utilized as the EGF after its moment was first estimated relative to an earlier Gofar CMT event; this CMT event was effectively used as a preliminary Green's function for the single EGF moment calculation. The other events in the swarm were then detected by cross-correlating the 2007 EGF waveform with seismograms from several GSN stations. Individual events were identified in the cross-correlation process as arrivals with a high cross-correlation coefficient at a number of stations sufficient to ensure azimuthal coverage. The relative locations of these newly detected events were determined using the same procedure as was used for the Galapagos and Siqueiros swarms.

2.3 Skew of moment release

Seismic swarms are distinguished from typical mainshock–aftershock sequences by their unique seismicity patterns: the largest swarm events tend to occur later in the sequence, swarms contain several large events as opposed to one clear mainshock, and elevated swarm seismicity is more prolonged in time (Fig. 2). Swarms thus deviate from established triggering models developed for aftershock sequences, such as Omori's law, which describes the decay rate of earthquakes following a mainshock (Omori 1894). Because of these deviations, quantitative earthquake triggering models such as the Epidemic Type Aftershock Sequence (ETAS) model (Ogata 1988) do not provide a good fit to the temporal evolution of moment release during a swarm (Llenos *et al.* 2009). One simple way to quantitatively identify earthquake clusters with swarm-like properties is through characterizing the timing of the largest earthquakes relative to the rest of the seismicity. To accomplish this, we calculate the skew of the seismic moment release history (i.e. the standardized third central moment) for each of the sequences that we analyse.

To calculate a skew value for a given sequence from its moment release history, we define the duration of the swarm as the period of time during which the seismicity rate is at least 20 per cent of its maximum value. This 20 per cent seismicity rate convention provides us with a consistent way to define the beginning (t_1) and end of the sequence. The seismicity rate is calculated here using 2-hr time bins. Moments used to determine the moment release history, $F(t) = \int_{t_1}^{t} M_o \mathrm{d}t$, are calculated using the definition of M_w (Kanamori 1977). For swarms in Southern California with local magnitudes (M_L) taken from SCEDC, we assume that M_L is equivalent to M_w. $F(t)$ is normalized so that within the determined time period of heightened seismicity $\lim_{t \to \infty} F(t) = 1$. The third central moment is then calculated as an integral over the duration of the sequence:

$$\bar{\mu}_3 = \int (t - t^*)^3 \, \mathrm{d}F(t), \tag{1}$$

where t^* is the centroid time (Jordan 1991). The skew of seismic moment release is represented by the standardized third central moment, which is equal to the third central moment divided by the standard deviation cubed, so that $skew = \bar{\mu}_3/\sigma^3$ (Panik 2005). Skew values quantitatively reflect the temporal evolution of the moment release during an earthquake sequence, with a value of zero for a symmetric sequence, a negative value for a sequence that begins slowly and ends abruptly, or a positive value for a sequence that begins abruptly and decays slowly, such as a typical
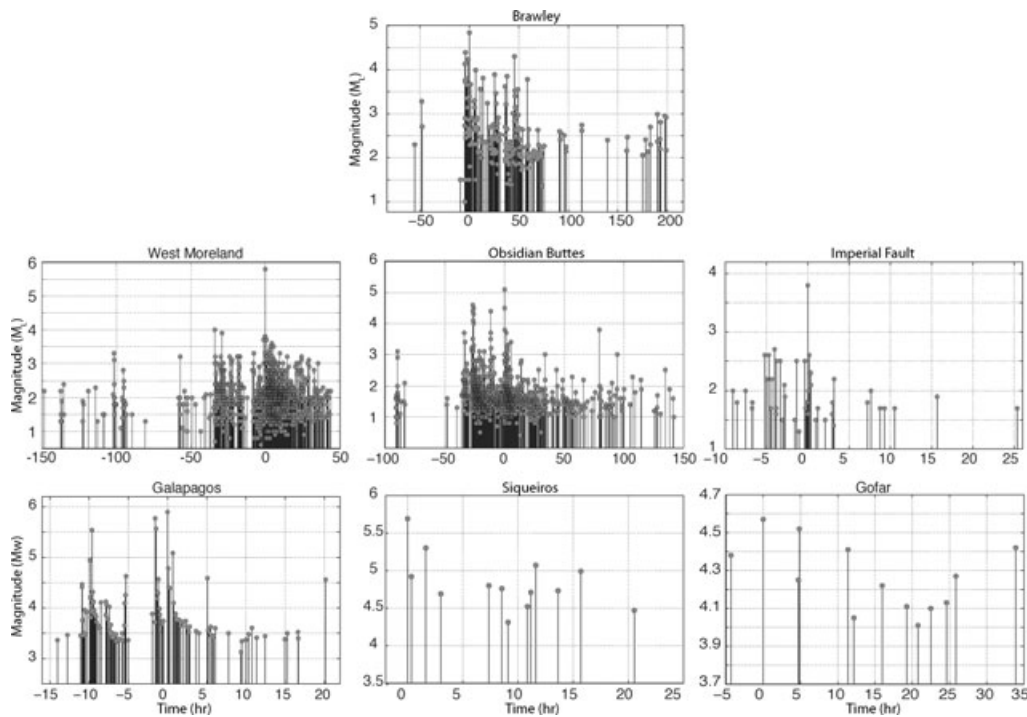
Figure 2. The seven transform earthquake swarms are displayed in terms of event times and magnitudes, with time in hours relative to the largest event. Seismicity patterns differ from those usually associated with mainshock–aftershock triggering. In several sequences the largest events occurred several hours after the onset of increased seismicity and multiple large events occurred rather than one distinct main shock.

mainshock–aftershock sequence. This value serves as a rough way of quantitatively differentiating swarm-like sequences from main shock–aftershock sequences (see Discussion).

2.4 Stress drop

To differentiate swarm and aftershock sequences based on their spatial properties, we calculate an effective seismic stress drop for each sequence. While stress drop values for large strike-slip earthquakes are on the order of 1–10 MPa (Kanamori 1994; Peyrat *et al.* 2001; Abercrombie & Rice 2005), the effective stress drop of swarms in Southern California tends to be an order of magnitude lower than mainshock–aftershock sequences (Vidale & Shearer 2006). We estimate the effective stress drop for each swarm using an approach similar to that of Vidale & Shearer (2006). Earthquake locations are used to make a rough approximation of the fault length as well as the fault width for events with reliable depth estimates. The cumulative moment of the sequence is calculated as the sum of the moments of the events in the sequence, which are estimated from catalogue reported values of M_L or M_w. We assume a vertical strike-slip fault and estimate stress drop as:

$$\Delta\sigma = \frac{2}{\pi}\mu\frac{\bar{D}}{w}, \qquad \text{with } \bar{D} = \frac{M_o}{\mu S} \qquad (2)$$

(Kanamori & Anderson 1975). Here, μ is the shear modulus, $\bar{D}$ is the average slip, w is the seismic width and $S = wL$ is the fault area with L equal to the fault length. For the swarms in Southern California, a rough estimate of width is made from the depths of the earthquakes and on the EPR transforms width is assumed to be 5 km (Trèhu & Solomon 1983).

3 RESULTS

3.1 1975 Brawley Swarm

In 1975 a large earthquake swarm occurred in the NW-striking Brawley seismic zone, just south of the Salton Sea. This swarm was analysed by Johnson & Hadley (1976) using data recorded by 16 short-period instruments that were part of the USGS Imperial Valley array. Locations were derived for 264 events spanning 8 d; the occurrence times and magnitudes of these events are displayed in the first panel of Fig. 2. Epicentres exhibit bilateral migration, spreading outward at a rate of approximately 0.5 km hr^{-1} (Johnson & Hadley 1976). A source model involving the propagation of a right-lateral creep event was hypothesized as an explanation for the hypocentral migration. Johnson and Hadley cited a number of observations as support for this model, including an increase in detected shallow seismicity directly before the onset of the swarm, as well as the existence of seismically quiescent fault segments in the region.

During the 1975 Brawley swarm, elevated seismicity levels persisted for over 100 hr after the largest events, resulting in a positive skew value of 1.8 (Table 1). Including the largest event, there were six earthquakes with moment magnitudes greater than 4.0, several of which preceded the largest, M_L 4.7 event. The effective stress drop calculated for this sequence using a fault length of 12 km and width of 9 km estimated from SCEDC catalogue locations is 0.032 MPa. Our estimate of fault length and width are consistent with the Johnson and Hadley estimate of the swarm's spatial extent, which was determined using local network data.

3.2 West Moreland and Obsidian Buttes swarms

The 1981 West Moreland swarm and 2005 Obsidian Buttes swarm also both occurred within the Brawley Seismic Zone. Events

Table 1. Southern California and RTF Swarm Seismicity parameters.

| Sequence	skew	Total M_w	Fault length	Width	Total stress drop	Approx. migration rate
Brawley 1975	+1.8	5.04	12 km	8 km	0.038 MPa	0.5 km hr^{-1} (Johnson & Hadley)
West Moreland 1981	−11.1	5.80	16 km	6 km	0.71 MPa	1.0 km hr^{-1} (Lohman & McGuire)
Obsidian Buttes 2005	−0.9	5.27	8 km	5 km	0.33 MPa	0.5 km hr^{-1} (Lohman & McGuire)
Imperial 2003	−1.6	3.84	2.5 km	2 km	0.047 MPa	0.5 km hr^{-1} (this study)
Galapagos 2000	−0.29	5.90	45 km	5 km	0.50 MPa	1.0 km hr^{-1} (this study)
Siqueiros 2001	+1.5	5.85	40 km	5 km	0.49 MPa	Uncertain
Gofar 2007	+0.5	5.05	25 km	5 km	0.049 MPa	∼0.5–1.0 km hr^{-1} (this study)
Hector Mine 1999	+33.3	7.1	85 km	10 km	4.31 MPa	–
San Simeon 2003	+16.7	6.50	35 km	10 km	1.30 MPa	–
Joshua Tree 1992	+8.11	6.11	20 km	10km	0.59 MPa	–
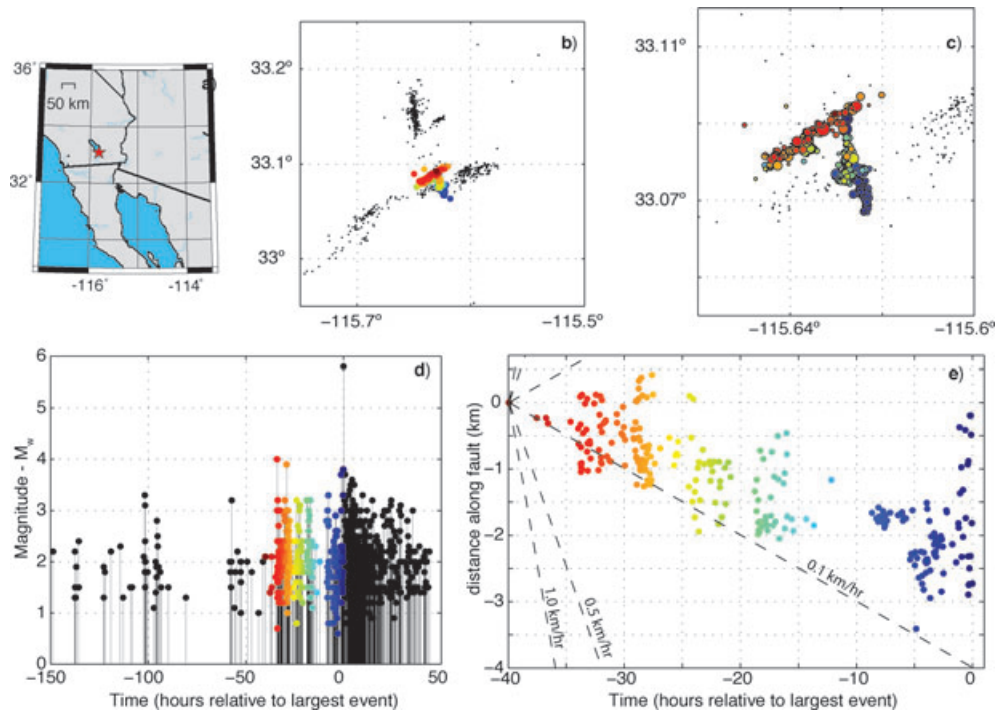
Figure 3. 1981 West Moreland swarm. (a) General geographic location of sequence south of the Salton Sea. (b) Event locations derived from *HypoDD* double-difference arrival time relocation algorithm (Lohman & McGuire 2007). In panels (b)–(e) colour indicates relative occurrence time of individual event. (c) Larger scale diagram of earthquake locations for events that occurred ∼30–0 hr before the largest event of the sequence. Bilateral hypocentral migration along a NE-striking fault early in this time period is followed by southward migration of events. (d) Local magnitude (M_L) versus time in hours relative to the largest event. (e) Distance along the fault plotted against occurrence time for events that occurred in the same −30–0 hr time period preceding the largest event. A migration rate of approximately 0.1 km hr^{-1} is apparent for events spreading southward along the NW striking fault.

associated with these sequences were recorded by the Southern California Seismic Network and were the focus of the study by Lohman & McGuire (2007). Peak seismicity during the West Moreland swarm spanned more than 3 d, and seismicity was elevated above the background rate for over 130 hr before the occurrence of the largest event, a M_w 5.9. Swarm events demonstrated a complicated hypocentral migration pattern. Early in the sequence, hypocentres spread bilaterally along a northeast–southwest striking fault and then migrate south within the seismic zone on along a northwest–southeast striking fault during the 30 hr preceding the largest event at a rate of about 0.1 km hr^{-1} (Fig. 3). Event migration is difficult to interpret following the largest swarm event because the rupture area associated with the M_w 5.9 obscures spatial patterns. Similar to the West Moreland swarm, bilateral migration was observed during the initial stages of the multiple day Obsidian Buttes swarm. Earthquake hypocentres demonstrate bilateral

spreading along the northeast-striking fault at a rate of approximately 0.5 km hr^{-1} during two distinct seismicity bursts that occurred approximately 35 and 25 hr before the largest swarm event (Fig. 4). Deformation associated with this swarm was also observed geodetically, using InSAR observations, and was recorded by two nearby Southern California Integrated GPS Network (SGIGN) stations. An inversion of the InSAR data demonstrated that significant shallow aseismic slip was required during the Obsidian Buttes swarm to explain the extent of surface deformation (Lohman & McGuire 2007).

We calculate skew values of −11.1 and −0.9 for the West Moreland and Obsidian Buttes swarms, respectively. These negative values result from a large amount of moment release before the sequences' temporal centroid, which is essentially coincident with the largest event. The negative skew values signify the ramping up of seismic activity before the largest events occur. The effective
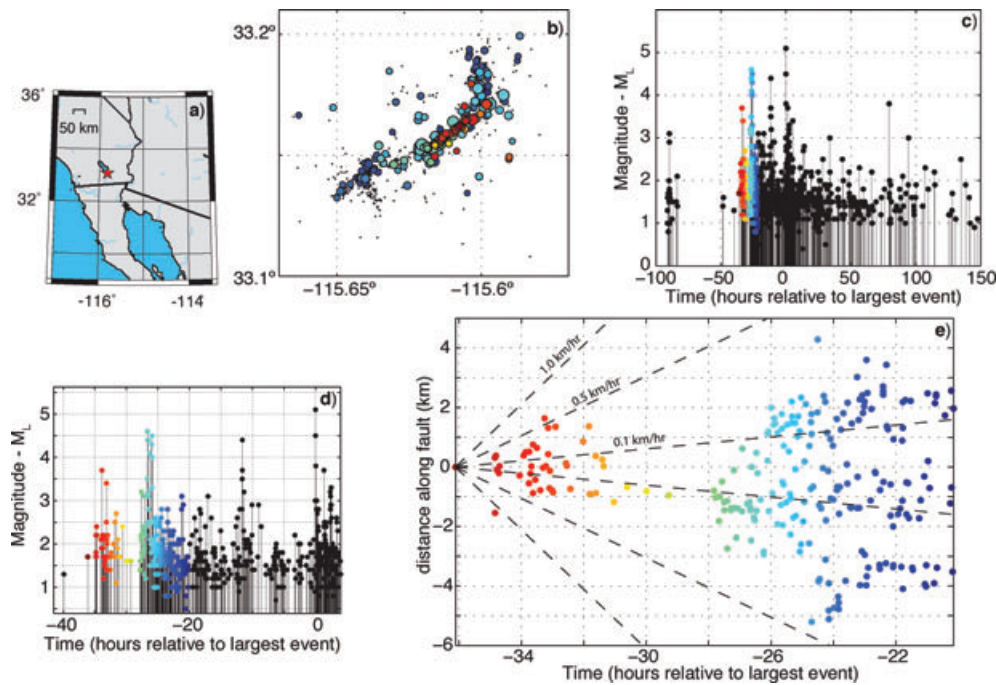
Figure 4. 2005 Obsidian Buttes swarm. (a) General geographic location. (b) Event locations derived from *HypoDD* double-difference arrival time relocation algorithm (Lohman & McGuire 2007). In panels (b)–(e) colour corresponds to relative occurrence time of event. (c) Local magnitude (M_L) versus time in hours relative to the largest event. (d) Larger scale time-magnitude plot highlights the time period preceding the largest event of the sequence ($\sim$−30 to −20 hr) when spatial migration is apparent along the NE-striking fault. (e) During this time period, hypocentres migrate bilaterally during two distinct seismicity bursts at a rate between 0.1 and 0.5 km hr^{-1}.

stress drop for these sequences was estimated at approximately 0.71 and 0.33 MPa, again relatively low compared to effective stress drop values typical of large mainshocks in the region.

3.3 2003 Imperial fault swarm

In 2003 May, an earthquake swarm occurred on a NE-striking fault within the Imperial fault zone. During this sequence, seismic activity was elevated for approximately 30 hr, with the largest earthquake, a M_L 3.8, occurring about 9 hr after the onset of elevated seismicity. Arrival times from the Mexican RESNOM and SCSN catalogues were combined and used to relocate swarm events. About 10 000 traveltime differences for pairs of events were used to relatively relocate 51 earthquakes from *P*- and *S*-wave arrivals observed from a combination of 46 Californian and Mexican stations (Fig. 5b). Event hypocentres focus onto a fault plane approximately 2.5 km long, with location errors of 10 m based on the SVD error analysis. Events of this sequence also demonstrate northward hypocentral migration along the fault, at a rate between 0.1 and 0.5 km hr^{-1} (Fig. 5). The skew value calculated for the moment release of the Imperial fault swarm is −1.6, again reflecting a pattern of abundant small-magnitude seismicity ramping up to the largest events. The effective stress drop was estimated at 0.047 MPa.

3.4 2000 Galapagos Swarm

In 2000 October a seismic swarm was recorded on a left-lateral transform fault offsetting the Galapagos Ridge, just north of the Galapagos Islands. One hundred and thirty eight events associated with this episode were recorded by the NOAA hydrophone array deployed in the eastern Pacific Ocean (Fox *et al.* 2001). Approximately, 5 hr after the onset of the swarm, a M_w 5.2 event occurred, followed by a decrease in moment release rate until approximately

hour 12, when a doublet (M_w 5.7 and 5.5) occurred. These were followed a few hours later by the largest event, a M_w 5.9. The two largest earthquakes had focal mechanisms calculated in Global CMT catalogue (Dziewonsk *et al.* 2003), both of which were strike slip. In total, 30 events greater than M_w 4.0 occurred before the seismicity rate abruptly returned to background levels, approximately 36 hr after the swarm began.

Events associated with the Galapagos swarm were located relative to an EGF that occurred on 10/21 at 15:52:53 UTC using the surface wave relative relocation method (see Section 2) with GSN waveform data from 19 stations. The EGF was the largest event of the sequence and had a M_w calculated in Global CMT catalogue (Dziewonsk *et al.* 2003). Twelve events with the best constrained centroid inversions have been used here to analyse the spatial characteristics of this swarm (Fig. 6). Based on these locations, bilateral hypocentral migration along the transform occurred at a rate between 0.1 and 1.0 km hr^{-1} (Fig. 7).

Seismicity associated with the Galapagos swarm was also recorded by an 11 station broad-band seismometer array, deployed on the Galapagos Islands (Hooft *et al.* 2003). Although the land-based seismometer array, located entirely to the south of the fault, and the hydrophone array, located entirely to the west of the fault, were not well placed for constraining Galapagos Ridge transform earthquake locations, they were useful for determining event magnitudes with a higher degree of accuracy than can be achieved from teleseismic data. Love-wave arrivals from rotated transverse-component records were identified using an EGF technique similar to that used with the teleseismic R1-arrivals, as described in Section 2. One hundred and nine events were detected with cross-correlation coefficients greater than 0.7 from seismograms filtered to 0.03–0.08 Hz. Magnitude estimates for these events are displayed in Fig. 7(c) as black symbols. Based on this Love-wave derived catalogue we
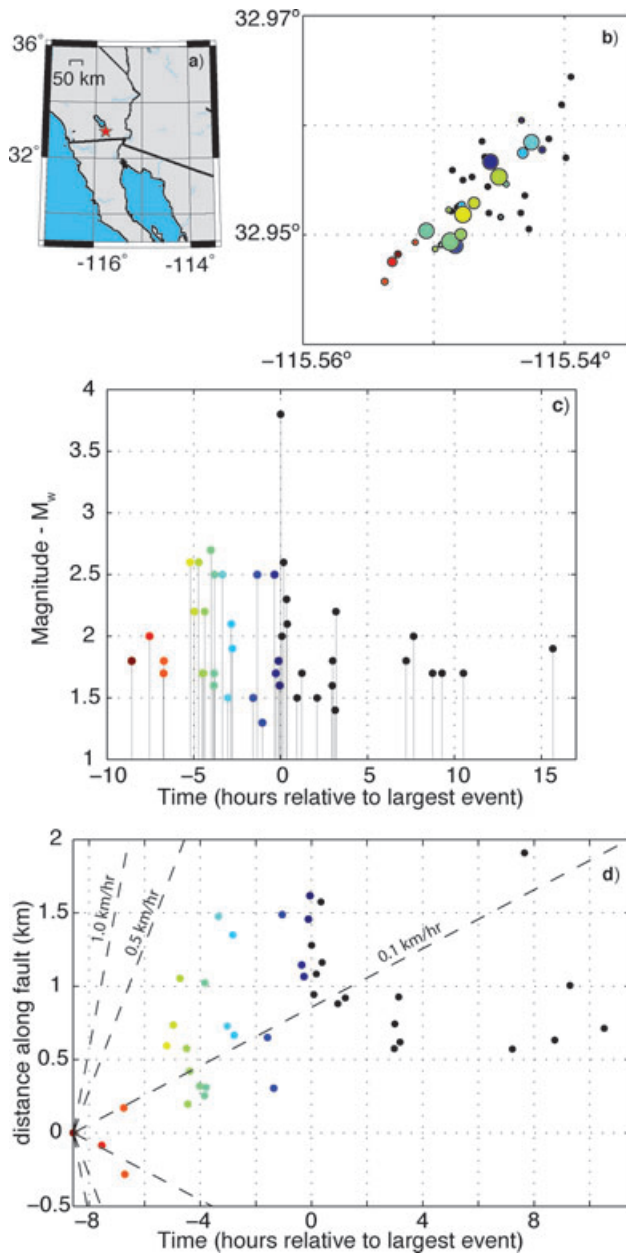
Figure 5. 2003 Imperial fault swarm. (a) General geographic location. (b) Event locations derived from *HypoDD* double-difference arrival time relocation algorithm using data from SCEDC (California) and RESNOM (Mexico) seismic arrays. In panels (b)–(d) colour corresponds to time of event. (c) Local magnitude versus time plot shows small magnitude seismicity ramping up to the largest event 10 hr into the sequence. (d) Hypocentres migrate unilaterally along the NE-striking fault from the southwest to the northeast at rates between 0.1 and 0.5 km hr^{-1}.

calculated a skew of -0.29, reflecting the significant amount of moment release that occurred before the largest event of the sequence. The cumulative moment from the Love-wave determined magnitudes was used with the fault length estimated from surface wave relocations to determine an effective stress drop of 0.50 MPa.

3.5 2001 Siqueiros swarm

A large earthquake sequence occurred on the Siqueiros transform fault in 2001 April and was also detected by the eastern Pacific

NOAA hydroacoustic array. One hundred and seventy *t*-phase events associated with the 2001 sequence were observed by hydrophones; these events were located on the S2 and S3 segments of the Siqueiros fault (Gregg *et al.* 2006, Fig. 8a). The largest event was a M_w 5.7, as calculated in the Global CMT catalogue (Ekström *et al.* 2003), which occurred very early in the sequence. With the CMT event as the Green's function, 13 events with magnitudes greater than 4.2 were detected and located using the surface wave method. Seismograms used in the centroid location inversions came from 21 GSN stations that were bandpass filtered to 0.02–0.04 Hz. Earthquake centroids clearly locate onto the two fault segments, however the spatial evolution of seismicity during the sequence is difficult to interpret (Fig. 8). During the first 8 hr following the largest event, centroids migrated from west to east along the S3 segment of the Siqueiros fault, corresponding to the first 45 *t*-phase events. Seismicity then became active on the S2 segment to the west, and again migrated east for the remainder of the episode. These two fault segments are separated by an intertransform spreading centre (ITSC). Gregg *et al.* (2006) proposed that some of the seismicity that occurred later and to the west was associated with secondary normal faults flanking the ITSC. While this may account for some of the smaller seismicity seen in the *t*-phase data, based on the surface wave locations and waveform similarity, the large events occurred as right-lateral strike-slip earthquakes, similar to the CMT catalogue event (Ekström *et al.* 2003). The skew of the Siqueiros sequence is positive, around $+1.5$, reflecting the occurrence of the largest event early in the sequences, followed by prolonged seismic activity. The total stress drop from earthquakes on both segments was calculated at approximately 0.49 MPa.

3.6 2007 Gofar swarm

The Gofar transform fault is the southernmost and most seismically active of the Quebrada-Discovery-Gofar fault system that offsets the EPR at approximately 4° south. In the end of 2007 December, a 2-d-long earthquake sequence was recorded on the eastern segment of the Gofar transform. Events associated with this sequence were detected and located using the R1 surface wave method, with data from 15 GSN stations. The location and magnitude of the empirical Green's function event used in this analysis were calculated relative to a CMT event that occurred on the same fault segment in 2003. The EGF used for locating the remainder of the sequence events was a M_w 5.3 that occurred on 12/29 at 00:48:00, approximately 5 hr after the the beginning of elevated swarm seismicity. The 13 events with the best surface wave derived centroid locations focus onto a 25 km long segment of the fault (Fig. 9). From these locations it appears that earthquakes spread bilaterally along the east–west striking fault at a rate of approximately 0.5–1.0 km hr^{-1}. This sequence has a skew of $+0.5$ and a stress drop of approximately 0.049 MPa.

3.7 Southern California distributed seismicity

In order to develop a basis for comparison in our analysis of earthquake swarms on transform boundaries, we combine our findings from the seven moderate-sized recent and historical sequences described above, to those recently published by Vidale & Shearer (2006). In their analysis of small seismicity clusters (burst radius <2 km) in Southern California, 71 seismic bursts were identified using data from the SHLK_1.01 catalogue of cross-correlation relocations (Shearer *et al.* 2005). Fourteen of these events were classified as aftershock sequences on the basis that they began with their
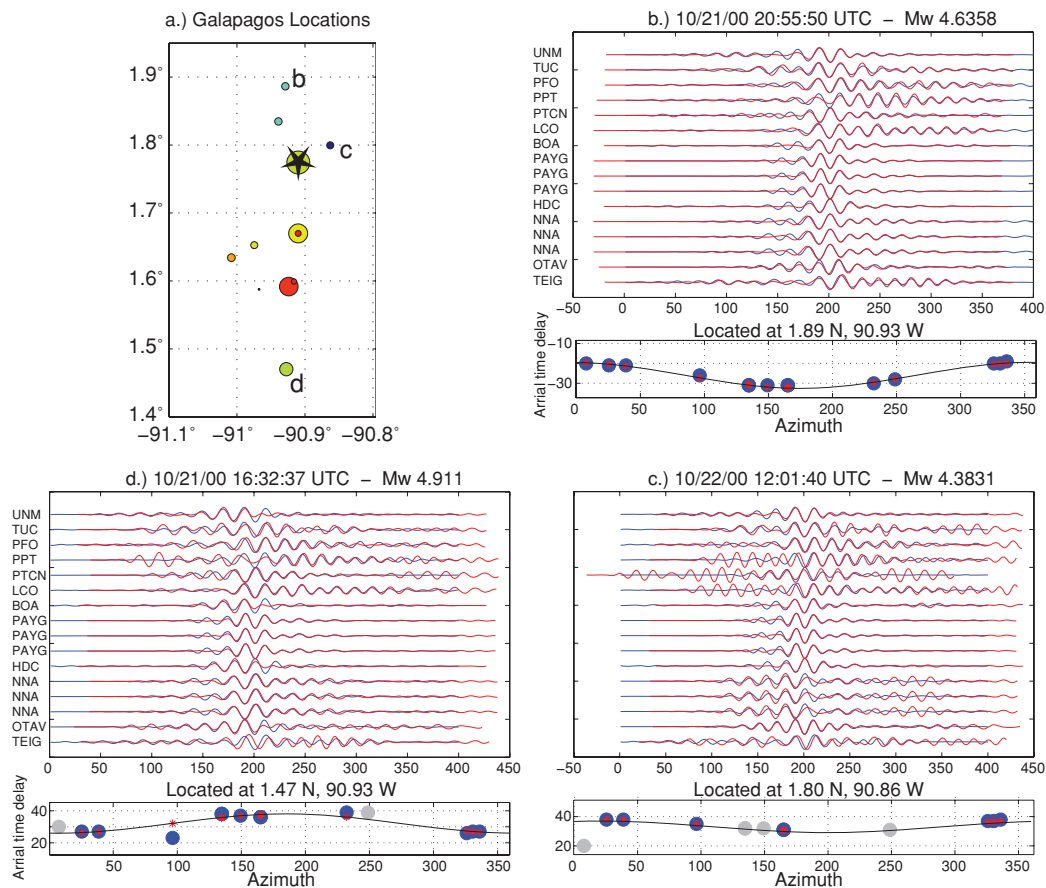
Figure 6. (a). Locations of events associated with the 2000 Galapagos sequence derived from R1 surface waves. Panels (b)–(d) illustrate three example centroid location inversions. The upper panel of each location figure demonstrates the empirical Green's function cross-correlation technique that was used to identify arrivals with similar focal mechanisms recorded at GSN stations. Blue lines represent the bandpass-filtered EGF waveform at each station, red lines represent waveforms of the event being located. Locations are derived by fitting a cosine function to relative arrival time delays from a set of azimuthally distributed stations. The cosine fit is displayed in lower panels of each location figure. The Green's function event used in this analysis is labelled with a star in panel (a). Events which located north of the Green's function event (b) and (c) are represented by an azimuth-dt cosine function with a 180° phase shift as compared to events that locate south of the Green's function event (d).

largest event, and 18 events were identified as swarm-like based on various qualitative factors. Specifically, swarms were recognized as episodes with the largest events occurring later into the sequence, large spatial extents relative to the largest earthquake (implying a low stress drop), and in many cases, a systematic spatial evolution of hypocentres, spreading either outward along the fault or linearly in one direction with time. We calculate skew and stress drop values for the 14 aftershock and 18 swarm-like sequences in the Vidale and Shearer data set; these are displayed in Fig. 10. Skew and stress drop values that were calculated for the seven swarms presented above are also displayed, as well as values for three large historical California earthquakes: Hector Mine, San Simeon and Joshua Tree and their aftershock sequences (Table 1). For all skew and stress drop calculations, swarms were defined using the 20 per cent seismicity rate cutoff convention for the temporal limits of swarm extent, outlined in Section 2. The estimated stress drop values for the Vidale and Shearer seismic bursts were calculated assuming circular faulting with a burst radius that is the mean of the distances to the events in each sequence form the centroid of the sequence (Vidale & Shearer 2006). The stress drop for the three large California aftershock sequences is calculated by estimating a fault length and width and assuming a vertical strike-slip fault, similar to the stress drop calculations made for the seven large swarms. Although these stress drop values should not be taken to be equivalent to effective stress drop values associated with a single large rupture, they do provide a means of approximately characterizing the ratio of moment release to rupture area. Fault length, width, stress drop and skew values are also presented in Table 1.

Based on the seismicity parameters displayed in Fig. 10, swarm-like sequences cluster toward the low stress drop-low skew quadrant of the plot, with most swarms displaying negative skew values or small positive values, below +5. Both the aftershock-like seismicity bursts and the large aftershock sequences meanwhile, cluster fairly regularly into the quadrant representative of higher stress drops and high positive skew values. These positive skew values reflect established empirical triggering patterns such as Omori's Law. The quantitative skew and stress drop parametrization of earthquake sequences presented in this way corresponds well with the Vidale and Shearer observational classification of a sequence being 'aftershock-like' or 'swarm-like' based on the duration and presence or lack of an initiating main shock, as well as the spatial extent.

4 DISCUSSION

Our analysis of the spacial and temporal characteristics of swarms on Southern California and EPR transform faults exposes three
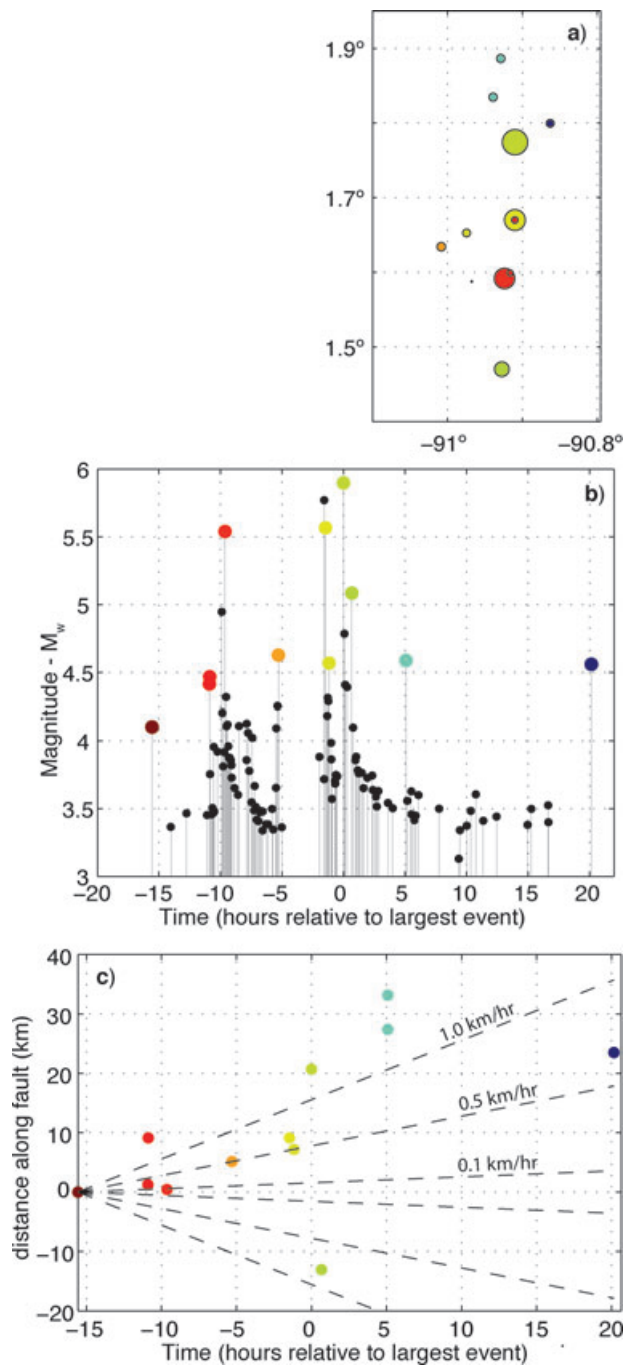
Figure 7. 2000 Galapagos Swarm (a) Centroid locations derived using R1 surface wave relocation method. Colour in panels (a)–(c) indicates time of event. (b) Time versus moment magnitude. Black symbols correspond to magnitudes derived from Love-wave cross-correlation using data from the Galapagos Islands seismometer array (Hooft *et al.* 2003). Coloured symbols correspond to events relocated using teleseismic R1 surface wave data. (c) Surface wave located events demonstrate northward migration along the Galapagos Ridge transform during the swarm at approximately 1.0 km hr^{-1}.
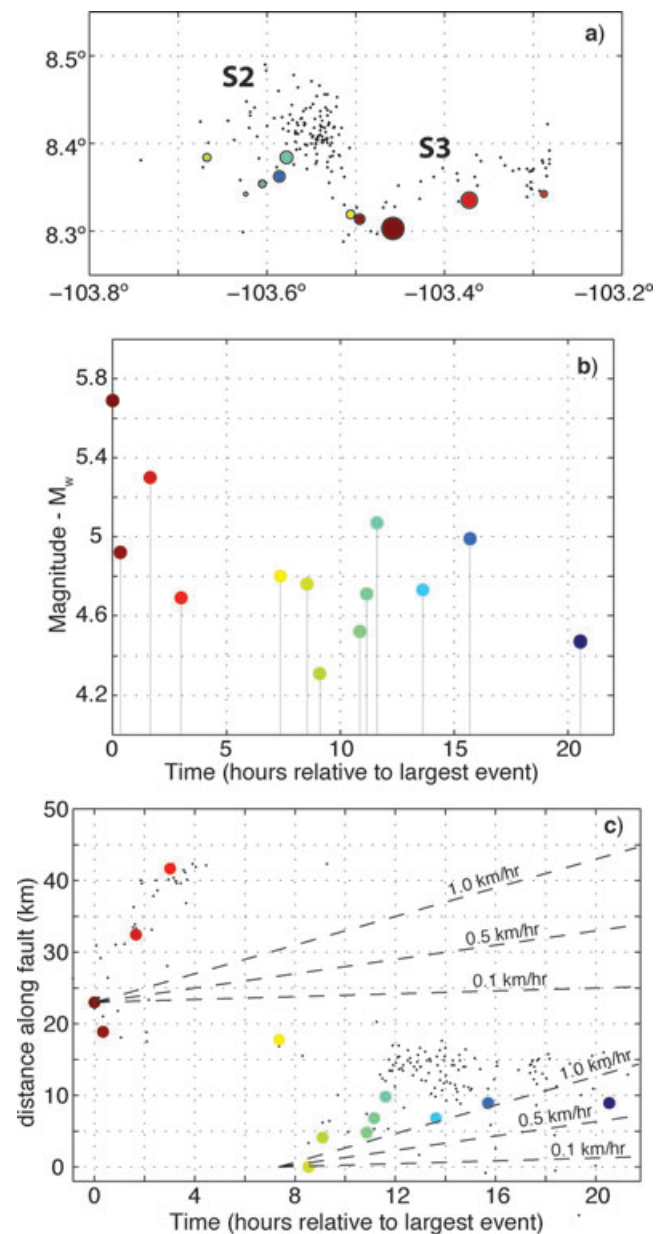

Figure 8. 2001 Siqueiros transform sequence. (a) Locations of events derived from surface wave relocation technique are displayed as coloured symbols. In panels (a)–(c) colour corresponds to occurrence time of individual events. Black dots represent *t*-phase data from the NOAA hydroacoustic catalogue. Earthquakes occurred on the S2 and S3 segments of the Siqueiros fault. (b) Time and moment magnitudes. (c) Seismicity demonstrates complex temporal-spatial migration patterns. During the swarm events migrated from west to east along the S3 segment, and then late in the sequence demonstrate migration again from west to east along the S2 segment at approximately 1.0 km hr^{-1}.

distinct properties of these sequences that signify a consistent physical driving mechanism. A deviation of the temporal evolution of moment-release from typical scaling laws (i.e. low skew), low effective stress drop values, and migration velocities of 0.1–1.0 km hr^{-1} are all consistent with a model in which aseismic fault slip modifies the stress-field and triggers swarm seismicity. Historical sur-

face deformation observations as well as recent geodetic studies in the Salton Trough have noted a prevalence of shallow creep events (Lyons *et al.* 2002; Lyons & Sandwell 2003; Lohman & McGuire 2007), demonstrating the feasibility of this mechanism for the Southern California faults. There have been no direct geodetic observations of creep on EPR transform faults, but it is well documented that oceanic transforms must have a significant component of aseismic fault slip (Bird *et al.* 2002; Boettcher & Jordan
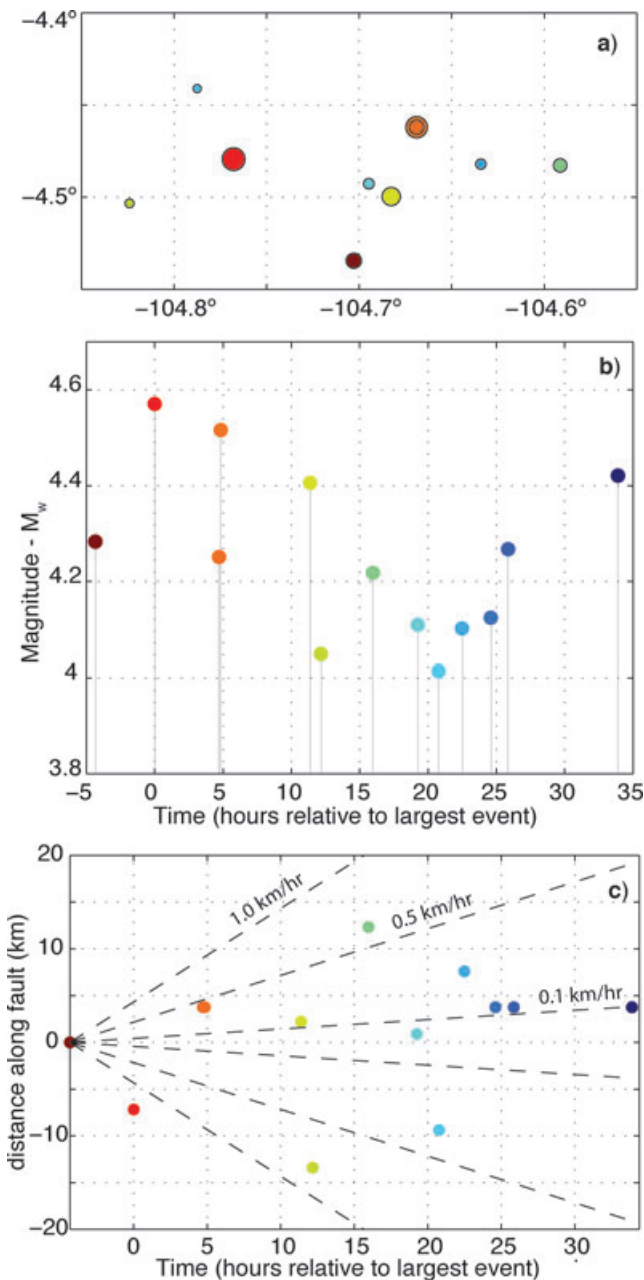
Figure 9. 2007 Gofar Swarm (a) Hypocentre locations derived using R1 surface wave location technique. In panels (a)–(c) colour corresponds to the occurrence time of individual events. (b) Time and moment magnitude of 13 large events. (c) Event centroid locations migrate along the eastern segment of the Gofar transform from west to east at a rate of approximately 0.5–1.0 km hr^{-1}.

2004), making creep a plausible explanation for the EPR swarms as well.

Many of the sequences examined here display a gradual ramping-up of moment release, with the largest events occurring late in the sequence, multiple large events and seismicity that is prolonged in time. These characteristic features of seismic swarms: the deviation from both the empirical Båth's Law and Omori-like temporal decay, are manifest into small positive or often negative skew values relative to those associated with aftershock sequences (Fig. 10). Especially when they are combined with observations of the characteristic spatial migration rate associated with swarms and low

seismic stress drop, anomalous skew values calculated here may indicate episodes in which seismicity deviates from aftershock-like Coulomb stress-triggering patterns, and is driven instead by a transient stressing event.

In order to quantitatively demonstrate the deviation from typical mainshock–aftershock triggering statistics that occurs during swarm-like bursts, Llenos *et al.* applied the empirical Epidemic-Type Aftershock Sequence (ETAS) model to a number of sequences and found that it could not fit swarm-like seismicity patterns (Llenos *et al.* 2009). The ETAS model combines empirical triggering laws, including Omori's Law, and has been used to represent the normal occurrence rate of earthquakes triggered by previous events (Ogata 1988; Helmstetter & Sornette 2003a). Here, we use the ETAS model to investigate how these empirical laws can be applied to simulate seismicity associated with the Galapagos swarm. We first optimize ETAS seismicity parameters over a 26-month time period preceding the large swarm in 2000 on the Galapagos Ridge transform fault. Values of the ETAS parameters are derived here as the maximum likelihood fit based on events greater than M_w 3.6 (the magnitude threshold of our surface wave derived catalogue) assuming an Omori time decay parameter, p, that is constrained to 1.0 (Bohnenstiehl *et al.* 2002) and the moment-distribution exponent, α, constrained to 0.8 (Boettcher & Jordan 2004; McGuire *et al.* 2005). For this fault, the best-fitting background seismicity rate is $\mu = 0.03$ earthquakes/d and local seismicity parameters $c = 0.01$ d and $K = 0.3$. In Fig. 11, the observed seismicity catalogue (blue line) of Galapagos events spanning 1999 May to 2002 September, including the 2000 swarm, is presented along with ETAS-predicted seismicity derived using the optimized parameters (red line). The seismicity is displayed in the form of the number of cumulative events versus ETAS-transformed time (Ogata 2005), which represents the amount of time predicted to elapse before the next seismic event based on the background seismicity rate and the aftershocks of previous seismicity. The observed seismicity deviates significantly from that which is predicted using the ETAS model during the period of the swarm (shaded region). Early in the sequence, the cumulative number of observed earthquakes far exceeds that predicted by the ETAS model, and then following the largest swarm event exhibits a relatively diminished rate compared to the ETAS prediction. Anomalous skew values, like the -0.29 skew of the Galapagos swarm, reflect these types of deviations, and indicate a triggering phenomenon that cannot be represented by a stationary stochastic model that emulates aftershock seismicity. Similar to the findings of the Llenos *et al.* study, this analysis indicates that in order to reproduce seismicity rates observed during swarms, an additional stressing phenomenon is required beyond the triggering associated with one seismic event triggering another.

The low effective stress drop values characteristic of swarms also provide evidence for a unique driving process. Values calculated for sequences here, on the order of 0.01–1.0 MPa, are lower than values for typical mainshock–aftershock sequences of similar size (i.e. 1–10 MPa). Recently, Brodsky & Mori (2007) demonstrated that creep events have lower stress drops than ordinary earthquakes, on the order of 0.1 MPa. Low effective stress drop values estimated for swarms in this study are thus consistent with values that would be expected for aseismic creep events. Assuming the 0.1 MPa value applies to creep events driving the EPR swarms as well, we can roughly estimate the magnitude of the aseismic slip. For the example of the Gofar sequence, with a fault length $L = 25$ km, width $w = 5$ km and stress drop $\Delta\sigma = 0.1$ MPa we find an aseismic moment release of approximately M_w 5.3. While this is clearly only a first order estimate, it suggests that aseismic slip during the EPR swarms
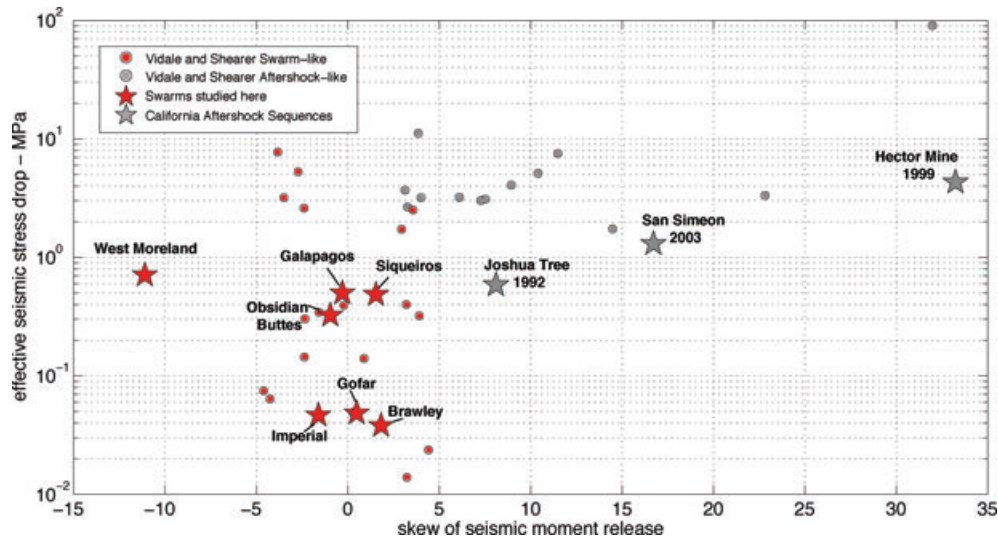
Figure 10. Comparison of calculated values of the skew of seismic moment release history and effective seismic stress drop for each of the seven sequences presented here along with those from the Vidale & Shearer (2006) analysis of seismic bursts in Southern California. Three large historical mainshock–aftershock sequences from California are also displayed for comparison purposes. Oceanic transform sequences and continental transform swarms from the Salton Trough (red stars) as well as the Vidale & Shearer 'swarm-like' bursts (red dots) trend toward the low skew-low stress drop quadrant of the parameter space. This differs from those values associated with the aftershock sequences shown (i.e. skew >5, $\Delta\sigma > {\sim}1$ MPa, grey stars and dots).

would be comparable in size to the seismic component, roughly agreeing with the long-term partitioning of slip between the two failure modes as seen in global studies of the slip deficit on oceanic transforms (Bird *et al.* 2002; Boettcher & Jordan 2004).

The relatively narrow range of spatial migration velocities between 0.1 and 1.0 km hr^{-1} may be the most direct evidence of aseismic fault slip. Observations of seismicity triggered by borehole fluid injection (Audigane *et al.* 2002; Shapiro *et al.* 2005) and subsurface fluid flow from magma degassing (Hainzl & Ogata 2005) consistently show earthquake hypocentres that spread following much slower pore-pressure diffusion, with distances that increase proportional to $t^{1/2}$ at rates not exceeding metres per day. Based on the migration rates seen here, the Salton Trough and EPR swarms are most likely not caused by fluid-flow transients. Geodetic observations further rule out magma intrusion in favor of fault slip (Lohman & McGuire 2007). Limited geodetic observations of propagation speeds associated with slow earthquakes and aseismic creep events are, to first order, consistent with migration rates between 0.1 and 1.0 km hr^{-1}. Studies using creepmeters to observe creep events on the San Andreas, Calaveras and Hayward faults determine propagation speeds on the order of 10 km d^{-1} (0.4 km hr^{-1}) (King *et al.* 1973; Burford 1977). More recently, borehole strainmeter observations of a slow earthquake sequence on the San Andreas were found to be consistent with rupture propagation rates between 0.2 and 0.35 ms^{-1} (0.7–1.3 km hr^{-1}) (Linde *et al.* 1996). In the Salton Trough, creep events from the Cerro Prieto stepover at the southern end of the Imperial fault have been observed with a rupture propagation velocity of 4 cm s^{-1} (0.14 km hr^{-1}) using multiple creepmeters (Glowacka *et al.* 2001). While data on creep rupture propagation velocity is limited due to sparse instrumentation, values from strike-slip faults in California and Mexico are within the range of our observations of seismicity migration rates.

Theoretical expressions relating stress drop, rupture propagation velocity and slip velocity provide the final link between earthquake swarms and aseismic creep events. Ida (1973) and Ohnaka and

Yamashita (1989) derived a relation between maximum slip velocity, $v_{\max}$, and rupture propagation velocity, v_r, for a mode II shear rupture propagating with a constant velocity of the form:

$$v_{\max} = \gamma \frac{\Delta\sigma_b}{\mu} v_r. \tag{3}$$

Here, γ is a constant on the order of one and $\Delta\sigma_b$ is the breakdown stress drop, which characterizes the difference between the the peak stress and stress level during frictional sliding (Shibazaki & Shimamoto 2007). Rate-state friction models were used by Rubin (2008) to determine essentially the same relation for a propagating rupture front with a quasi-steady shape

$$\frac{v_r}{v_{\max}} = \frac{\mu}{\Delta\sigma}, \quad \text{and} \quad \Delta\sigma = \frac{b\sigma}{\ln[v_{\max}\theta/D_c]}, \tag{4}$$

with θ representing the 'state' ahead of the propagating front, D_c, the characteristic slip distance for state evolution, b, a lab-derived friction parameter that characterizes the drop in friction from peak to steady-state sliding levels and σ the effective normal stress. Using this relation for slip and rupture propagation velocity with approximate values derived from our analyses of swarm seismicity, $\Delta\sigma \sim$ 0.1 MPa, $v_r \sim 0.5$ km hr$^{-1} \sim 0.14$ m s^{-1} (Table 1) and the shear modulus $\mu = 30$ GPa, we derive a maximum slip velocity, $v_{\max} \sim 5 \times 10^{-7}$ m s^{-1}. This value is significantly slower than slip speeds during typical earthquakes, which are on the order of metres per second, but is comparable to surface displacement rates observed during creep events. On the Imperial fault, Glowacka *et al.* (2001) observed peak slip-rates using creepmeters on the order of 100 mm d^{-1} (10^{-6} m s^{-1}) during creep transients. Based on these relations, as long as the dominant slip mode is aseismic creep ($v_{\max} \sim 10^{-7}$ m s^{-1}) rather than seismic fault slip ($v_{\max} \sim 1$ m s^{-1}), our estimates of stress drop and rupture propagation velocity provide a self-consistent model of fault failure with either crack or rate-state equations. These calculations are also consistent with geodetic observations of shallow aseismic creep in the Salton Trough. By applying our estimate of rupture propagation velocity ($v_r = 0.28$ m s^{-1},
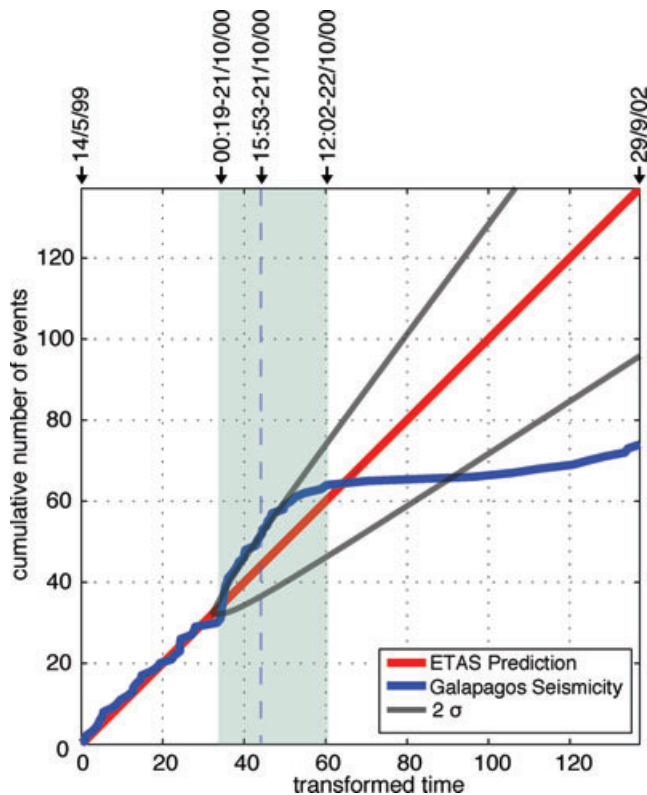
Figure 11. ETAS-transformed time versus cumulative number of events that occurred on the Galapagos Ridge transform fault from 1999 May to 2002 September. The seismicity rate predicted by the ETAS model is dependent on the time elapsed since the last event as well as the occurrence times and magnitudes of other previous events and the background seismicity rate (Ogata 1988). Maximum likelihood estimates of ETAS parameters derived here ($\mu = 0.03$ events/d, c $= 0.01$ d and $k = 0.3$) are optimized for the first 26 month time period with p and α constrained to 1.0 and 0.8, respectively. We assume a lower magnitude threshold of M_w 3.6. The best-fitting ETAS parameters are used to extrapolate the predicted cumulative number of events for the entire data set (red line). Blue line represents observed data. A significant deviation from the ETAS prediction is associated with the 2-d earthquake swarm in 2000 October (shaded region). The largest event of that sequence, a M_w 5.9 at 15:53 on October 21, is indicated with dotted line. Grey lines represent the 2σ confidence interval for the extrapolation of the ETAS prediction beyond the optimization time period assuming a standard Brownian process with a linear trend slope of 1 (Ogata 2005).

for the Obsidian Buttes swarm) and the observed slip velocity of Salton Trough creep events, $v_{max} \sim 10^{-6}$ m s^{-1} (Glowacka *et al.* 2001) with laboratory values of $b \sim 10^{-2}$, a density of 2500 kg m^{-3}, an S-wave velocity of 2.7 km s^{-1} (i.e. a shear modulus of 19 GPa) and a representative value of $\ln[v_{max}\theta/D_c]$ of 5 (Rubin 2008), eq. (4) yields a normal stress of 33 MPa. This value matches the expected effective normal stress for hydrostatic conditions at a depth of 2.3 km. Lohman & McGuire (2007) found the peak aseismic slip during the Obsidian Buttes swarm occurred between depths of 1 and 3 km. By combining this observation with the calculations made using the rate and state friction expression and seismicity parameters associated with swarms studied here, we find that the observed rupture propagation velocity of the Salton Trough and EPR swarms and a slip velocity on the order of that assumed for aseismic creep are consistent with laboratory derived values of the rate-state friction parameter $b \sim 0.01$ (Kilgore *et al.* 1993) as long as the Salton Trough faults fail under hydrostatic conditions.

Similarities between our findings and recent observations of silent slip and episodic slow slip transients in subduction zones bring up the question of whether or not these two phenomena could be related. Along strike propagation velocities have been observed for tremor and episodic slow slip (~ 0.2–0.7 km hr^{-1}, Obara 2002; Kao *et al.* 2006; Dragert *et al.* 2006) that are remarkably similar to those observed here associated with swarms on transform faults. This is surprising when it is considered in the context of the rate and state relations outlined in eq. (4) because tremor is believed to occur along the deep unstable-stable transition zone of the slab interface, around 30–40 km, and assuming a similar v_{max}, confining stress conditions there would require a drastically different propagation velocity as compared to our shallow (2–5 km) transform slip. Recent modeling of short-interval silent slip events by Shibazaki & Shimamoto (2007) as well as laboratory friction data for gabbro and GPS observations that have been applied to rate and state models by Liu & Rice (2009) however, have demonstrated that episodic slow slip like that observed along subduction zone interfaces can only be reproduced using numerical models if the effective normal stress (σ) along the fault is greatly reduced by a near-lithostatic pore pressure. With this requirement, effective normal stress conditions appropriate for deep-subduction zone slow slip transients are similar to stress conditions along the shallow transform faults we consider.

5 CONCLUSIONS

Based on our analysis of seismic swarms on Southern California and EPR transform faults, we have identified several parameters that point to aseismic creep as the likely driving mechanism for the recurrent swarms on these strike-slip plate boundaries. Swarms show a large spatial extent relative to their cumulative seismic moment and a correspondingly low effective stress drop, a temporal evolution that is inconsistent with standard scaling laws and spatial migration speeds on the order of 0.1–1.0 km hr^{-1}. These characteristics are consistent with field observations of creep events as well as with theoretical models of fault slip at creep rates. Given the relative frequency of swarms in the Salton Trough and EPR, it appears likely that a significant fraction of moderate and large earthquakes on these boundaries are triggered by aseismic fault slip. Moreover, all three properties of swarms could be easily identified in real time if high precision locations were available. In view of the significant damage Salton Trough swarms have caused in the past, these systematic properties could be used to improve real-time hazard estimates by detecting the existence of a swarm-like sequence relatively early in its evolution and identifying the increased level of hazard compared to a typical aftershock sequence.

REFERENCES

Abercrombie, R.E. & Rice, J.R., 2005. Can observations of earthquake scaling constrain slip weakening, *Geophys. J. Int.,* **162,** 406–424.

Audigane, P., Royer, J.J. & Kaieda, H., 2002, Permeability characterization of the Soultz and Ogachi large-scale reservoir using induced microseismicity, *Geophysics.,* **67,** 204–211.

Bird, P., Kagan, Y.Y. & Jackson, D.D., 2002. Plate tectonics and earthquake potential of spreading ridges and oceanic transform faults, in *Plate Boundary Zones, AGU Monograph,* **Vol. 30,** eds Stein, S. & Freymueller, J.T., pp. 203–218, Geodyn. Ser.

Boettcher, M.S. & Jordan, T.H., 2004. Earthquake scaling relations for mid-ocean ridge transform faults, *J. geophys. Res.* **109**(B12), B12302, doi:10.1029/2004JB003110.

Bohnenstiehl, D.R., Tolstoy, M., Dziak, R.P., Fox, C.G. & Smith, D.K., 2002. Aftershock sequences in the mid-ocean ridge environment: an analysis using hydroacoustic data, *Tectonophysics,* **354,** 49–70.

Brodsky, E.E. & Mori, J., 2007. Creep events slip less than ordinary earthquakes, *Geophys. Res. Lett.,* **34,** L16309, doi:10.1029/2007GL030917.

Brune, J.N. & Allen, C.R., 1967. A low-stress-drop, low-magnitude earthquake with surface faulting: the Imperial, California, earthquake of March 4, 1966, *Bull. seism. Soc. Am.,* **57,** 501–514.

Burford, R.O., 1977. Bimodal distribution of creep event amplitudes on the San Andreas fault, California, *Nature,* **268,** 424–426.

Castro, R.R. & RESNOM Working Group, 1998. P- and S- Wave Site Response of the Seismic Network RESNOM Determined from Earthquakes of Northern Baja California, Mexico, *Pure appl. geophys.,* **152,** 125–138.

Dragert, H., Wang, K. & Rogers, G., 2004, Geodetic and seismic signatures of episodic tremor and slip in the northern Cascadia subduction zone, *Earth Planets Space,* **56,** 1143–1150.

Dziewonski, A.M., Ekström, G. & Maternovskaya, N.N., 2003. Centroid-moment tensor solutions for October–December 2000, *Phys. Earth planet. Inter.,* **136,** 145–163.

Ekström, G., Dziewonski, A.M., Maternovskaya, N.N. & Nettles, M., 2003. Global seismicity of 2001: centroid-moment tensor solutions for 961 earthquakes, *Phys. Earth planet. Inter.,* **136,** 165–185.

Forsyth, D.W., Yang, Y., Mangriotis, M.D. & Shen, Y., 2003. Coupled seismic slip on adjacent oceanic transform faults *Geophys. Res. Lett.,* **30**(12), 1618, doi:10.1029/2002GL016454.

Fox, C.G., Matsumoto, H. & Lau, T.K.A., 2001. Monitoring Pacific Ocean seismicity from an autonomous hydrophone array, *J. geophys. Res.,* **106,** 4183–4206.

Glowacka, E., Gonzalez, J.J., Nava, F.A., Farfan, F. & Díaz de Cossio, G., 2001. Monitoring surface deformation in the Mexicali Valley, BC, Mexico, *Paper presented at the 10th FIG International Symposium on Deformation Measurements,* CA. Inst. of Technol., Orange, CA.

Gregg, P.M., Lin, J. & Smith, D.K., 2006. Segmentation of transform systems on the East Pacific Rise: implications for earthquake processes at fast-slipping oceanic transform faults, *Geology,* **34**(B05S07), 289–292.

Hainzl, S. & Ogata, Y., 2005. Detecting fluid signals in seismicity data through statistical earthquake modeling, *J. geophys. Res.,* **110,** B05S07, doi:10.1029/2004JB003247.

Helmstetter, A., Sornette, D., 2003a. Importance of direct and indirect triggered seismicity in the ETAS model of seismicity, *Geophys. Res. Lett.,* **30**(11), 1576–1579.

Helmstetter, A., Sornette, D., 2003b. Bath's law Derived from the Gutenberg-Richter law and from Aftershock Properties *J. geophys. Res.,* **30**(20), 2069–2072, doi:10.1029/2003GL018186.

Hill, D.P., 1977. A model for earthquake swarms, *J. geophys. Res.* **82,** 1347–1352.

Hooft, E.E., Toomey, D.R. & Solomon, S.C., 2003. Anomalously thin transition zone beneath the Galápagos hotspot, *Earth planet. Sci. Lett.,* **216,** 55–64.

Johnson, C.E. & Hadley, D.M., 1976. Tectonic implications of the Brawley earthquake swarm, Imperial Valley, California, January 1975, *Bull. seism. Soc. Am.,* **66,** 1133–1144.

Jordan, T.H., 1991. Far-field detection of slow precursors to fast seismic ruptures, *Geophys. Res. Lett.,* **18,** 2019–2022.

Kanamori, H., 1977. Energy release in great earthquakes, *J. geophys. Res.* **82**(20), 2981–2987.

Kanamori, H., 1994. Mechanics of earthquakes, *Ann. Rev. Earth Planet. Sci.,* **22,** 207–237, doi:10.1146/annurev.ea.22.050194.001231.

Kanamori, H. & Anderson, D.L., 1975. Theoretical basis of some empirical relations in seismology, *Bull. seism. Soc. Am.,* **65,** 1073–1095.

Kao, H., Shan, S., Dragert, H., Rogers, G., Cassidy, J.F., Wang, K., James, T.S. & Ramachandran, K., 2006. Spatial-temporal patterns of seismic tremors in northern Cascadia. *J. geophys. Res.,* **111,** B03309, doi:10.1029/2005JB003727.

Kilgore, B.D., Blanpied, M.L. & Dieterich, J.H., 1993. Velocity dependent friction of granite over a wide range of conditions, *Geophys. Res. Lett.,* **274,** 355–360.

King, C.Y., Nason, R.D. & Tocher, D., 1973. Kinematics of fault creep, *Phil. Trans. Roy. Soe. Lond., Ser. A.,* **274,** 355–360.

Linde, A.T., Gladwin, M.T., Johnston, M.J.S., Gwyther, R.L. & Bilham, R.G., 1996. A slow earthquake sequence on the San Andreas fault, *Nature,* **383,** 65–68.

Liu, Y. & Rice, J., 2009. Slow slip predictions based on gabbro friction data compared to GPS measurements in northern Cascadia, *J. geophys. Res.,* submitted.

Llenos, A.L., McGuire, J.J. & Ogata, Y., 2009. Modeling Seismic Swarms Triggered by Aseismic Transients, *Earth planet. Sci. Lett.,* **281,** 59–69.

Lohman, R.B. & McGuire, J.J., 2007. Earthquake swarms driven by aseismic creep in the Salton Trough, California, *J. geophys. Res.,* **112,** B04405, doi:10.1029/2006JB004596.

Lyons, S. & Sandwell, D., 2003. Fault creep along the southern San Andreas from interferometric synthetic aperture radar, permanent scatterers, and stacking, *J. geophys. Res.,* **108**(B1), 2047, doi:10.1029/2002JB001831.

Lyons, S.N., Bock, Y. & Sandwell, D.T., 2002. Creep along the imperial fault, southern California, from GPS measurements, *J. geophys. Res.,* **107**(B10), doi:10.1029/2001JB000763.

Magistrale, H., Day, S., Clayton, R.W. & Graves, R., 2000. The SCEC southern California reference three-dimensional seismic velocity model Version 2, *Bull. seism. Soc. Am.,* **90,** S65–S76.

McGuire, J.J., 2008. Seismic cycles and earthquake predictability on east pacific rise transform faults, *Bull. seism. Soc. Am.,* **98,** 1067–1084.

McGuire, J.J. & Segall P., 2003 Imaging of aseismic fault slip transients recorded by dense geodetic networks, *Geophys. J. Int..,* **155,** 778–788.

McGuire, J.J., Boettcher, M.S. & Jordan, T.H., 2005. Foreshock sequences and short-term earthquake predictability on East Pacific Rise transform faults, *Nature,* **434,** 457–461.

Nishimura, C.E. & Forsyth, D.W., 1988. Rayleigh wave phase velocities in the Pacific with implications for azimuthal anisotropy and lateral heterogeneities, *Geophys. J.,* **94,** 479–501.

Obara, K., 2002. Nonvolcanic deep tremor associated with subduction in southwest Japan, *Science,* **296,** 1679–1681.

Ogata, Y., 1988. Statistical models for earthquake occurrences and residual analysis for point processes, *J. Am. Stat. Assn.* **83,** 9–27.

Ogata, Y., 2005. Detection of anomalous seismicity as a stress change sensor, *J. geophys. Res.,* **110**(B5), B05506, doi:10.1029/2004JB003245.

Omori, F., 1894. On the aftershocks of earthquakes, *J. Coll. Sci. Imp. Univ. Tokyo.,* **7,** 111–200.

Panik, M.J., 2005. *Advanced Statistics from an Elementary Point of View,* Elsevier Academic Press, Amsterdam.

Peyrat S., Olsen, K. & Madariaga, R., 2001. Dynamic modeling of the 1992 Landers Earthquake, *J. geophys. Res.,* **106**(B11), 26 467–26 482.

Richter, C.F., 1958. *Elementary Seismology,* W.H. Freeman, San Francisco, CA.

Rubin, A.M., 2008. Episodic slow slip events and rate-and-state friction. *J. geophys. Res.,* **113,** B11414, doi:10.1029/2008JB005642.

Shapiro, S.A., Rentsch, S. & Rothert, E., 2005. Characterization of hydraulic properties of rocks using probability of fluid-induced microearthquakes, *Geophysics.,* **70,** F27–F33.

Shearer, P.M., 1997. Improving local earthquake locations using the L1 norm and waveform cross correlation: application to the Whittier Narrows, California, aftershock sequence, *J. geophys. Res.,* **102,** 8269–8283.

Shearer, P.M., Hauksson, E. & Lin, G., 2005. Southern California hypocenter relocation with waveform cross-correlation. Part 2: results using source-specific station terms and cluster analysis, *Bull. seism. Soc. Am.,* **95,** 904–915.

Shibazaki, B. & Shimamoto, T., 2007, Modelling of short-interval silent slip events in deeper subduction interfaces considering the frictional properties at the unstablestable transition regime, *Geophys. J. Int.,* **171,** 191–205.

Smith, K.D., von Seggern, D., Blewitt, G., Preston, L., Anderson, J.G., Wernicke, B.P. & Davis, J.L., 2004. Evidence for deep magma injection beneath Lake Tahoe, Nevada-California, *Science,* **305,** 1277–1280.

Trèhu, A.M. & Solomon, S.C., 1983. Earthquakes in the Orozco transform zone; seismicity, source mechanisms, and tectonics, *J. geophys. Res.,* **88,** 8203–8225.

Vidale J.E. & Shearer, P.M., 2006. A survey of 71 earthquake bursts across southern California: exploring the role of pore fluid pressure fluctuations and aseismic slip as drivers, *J. geophys. Res.,* **111,** B05312, doi:10.1029/2005JB004034.

Vidale J.E., Boyle, K.L. & Shearer, P.M., 2006. Crustal earthquake bursts in California and Japan: their patterns and relation to volcanoes, *Geophys. Res. Lett.,* **33,** L20313, doi:10.1029/2006GL027723.

Waldhauser, F. & Ellsworth, W.L., 2000. A Double-Difference Earthquake Location Algorithm: method and application to the Northern Hayward Fault, California, *Bull. seism. Soc. Am.,* **90,** 1353–1368.